Steel and Composite Structures, *Vol. 27, No. 3 (2018) 255-271*
DOI: https://doi.org/10.12989/scs.2018.27.3.255

Elastodynamic and wave propagation analysis in a FG graphene platelets-reinforced nanocomposite cylinder using a modified nonlinear micromechanical model

Seyed Mahmoud Hosseini [*1] and Chuanzeng Zhang [2a]

[1] *Industrial Engineering Department, Faculty of Engineering, Ferdowsi university of Mashhad, PO Box:91775-1111, Mashhad, Iran*
[2] *Department of Civil Engineering, University of Siegen, Paul-Bonatz-Str. 9-11, D-57076 Siegen, Germany*

(*Received October 8, 2017, Revised February 16, 2018, Accepted March 3, 2018*)

Abstract. This paper deals with the transient dynamic analysis and elastic wave propagation in a functionally graded graphene platelets (FGGPLs)-reinforced composite thick hollow cylinder, which is subjected to shock loading. A micromechanical model based on the Halpin-Tsai model and rule of mixture is modified for nonlinear functionally graded distributions of graphene platelets (GPLs) in polymer matrix of composites. The governing equations are derived for an axisymmetric FGGPLs-reinforced composite cylinder with a finite length and then solved using a hybrid meshless method based on the generalized finite difference (GFD) and Newmark finite difference methods. A numerical time discretization is performed for the dynamic problem using the Newmark method. The dynamic behaviors of the displacements and stresses are obtained and discussed in detail using the modified micromechanical model and meshless GFD method. The effects of the reinforcement of the composite cylinder by GPLs on the elastic wave propagations in both displacement and stress fields are obtained for various parameters. It is concluded that the proposed micromechanical model and also the meshless GFD method have a high capability to simulate the composite structures under shock loadings, which are reinforced by FGGPLs. It is shown that the modified micromechanical model and solution technique based on the meshless GFD method are accurate. Also, the time histories of the field variables are shown for various parameters.

Keywords: graphene platelets; generalized finite difference method; micromechanical model; wave propagation; shock loadings; reinforced structures

1. Introduction

To increase the mechanical strength of structures against dynamic and shock loadings, structures made of the reinforced composite materials are often applied. For the reinforcement of composite structures, it is beneficial to employ carbon nanotubes (CNTs), which are dispersed uniformly or non-uniformly within the matrix of composite materials. There are some recent research works in which the reinforced composite structures by CNTs have been studied using various numerical methods. Ghayumizadeh *et al*. (2013) studied the elastic wave propagation in a functionally graded nanocomposite cylinder reinforced by carbon nanotubes using the meshless local Petrov-Galerkin (MLPG) method. They assumed that the CNTs were distributed non-uniformly across the thickness of the cylinder along the radial direction. In another work, Ghouhestani *et al*. (2014) employed the MLPG method for dynamic analysis of multilayer functionally graded nanocomposite cylinders reinforced by carbon nanotubes subjected to shock loading. Hosseini (2013, 2014a) studied the effects of the reinforcement by CNTs on the natural frequencies and elastic wave propagation in a functionally graded nanocomposite cylinder reinforced by carbon nanotubes, respectively. He used a hybrid meshless method based on the generalized finite difference (GFD) and Newmark finite difference methods.

In recent years, some research works on the carbon nanotube reinforced-functionally graded (CNTR-FG) composite structures have been reported in literature. Some of them were focused on the geometrically nonlinear analysis (Zhang *et al*. 2016, Lei *et al*. 2017), buckling and stability analysis (Kiani 2016, Duc *et al*. 2017 and Shokravi 2017), bending characteristic of SWCNT-reinforced FG composite plates (Chavan and Lal 2017), dynamic analysis and size-dependence analysis of the CNTR-FG composite structures (Zhang 2017, Zhang *et al*. 2017a, b, Allahkarami *et al*. 2017 and Kiani 2017). In the above research works, various computational methods have been used to solve the corresponding problems such as the element-free IMLS-Ritz method and the isogeometric analysis (IGA). The material properties of the CNTR-FG composite structures were usually considered as effective material properties based on the rule of mixture.

Recently, the graphene platelets (GPLs) are also used as the reinforcement of composite structures. Verma *et al*. (2014) presented a review and discussed the different methods of manufacturing reinforced composites with graphene and also their properties (such as electrical,

*Corresponding author, Ph.D., Associate Professor,
E-mail: sm_hosseini@um.ac.ir
[a] Ph.D., Professor

ISSN: 1229-9367 (Print), 1598-6233 (Online)

mechanical and thermal properties). Many references to the previous works on the material properties and processing were given in this review. The intrinsic tensile strength of graphene is about 130 GPa and its elastic modulus is about 1 TPa, and also there is another specific characteristic, which is called the specific surface area with a value up to 2630 m^2g^{-1} (Yang *et al*. 2017). In the previously published works, it was reported that the GPLs have excellent mechanical and physical properties (Verma *et al*. 2014 and Yang *et al*. 2017). Furthermore, some recent research works were carried out to study the effects of the reinforced composite structures by GPLs on the static and dynamic behaviors of the structures using various solution techniques, such as the nonlinear free vibration (Feng *et al*. 2017a), nonlinear bending (Feng *et al*. 2017b), post-buckling (Chen *et al*. 2017), elastic buckling (Kitipornchai *et al*. 2017a), free and forced vibration (Song *et al*. 2017) and the nonlinear elastic moduli (Elmarakbi *et al*. 2016). To evaluate some elastic properties of the reinforced nanocomposites by CNT and graphene, Kumar and Srivastava (2016) employed the continuum based 3D representative volume element (RVE). One of the most important issues in the above cited research works is the determination of the effective mechanical properties of the nanocomposite structures reinforced by GPLs. To do this, two main micromechanical models were used in the above referenced papers, which are the Halpin-Tsai micro-mechanical model for the elastic moduli and the rule of mixture. In both micromechanical models, the volume fraction of GPLS was assumed to be uniform or vary linearly along certain directions (e.g., along the thickness direction of nanocomposite plates or cylinders).

In the above addressed research works, various solution techniques have been employed to solve the governing equations of the problems. One of the effective solution techniques is the GFD method. The GFD method has been successfully used by one of the authors for the study of the natural frequencies and the elastic wave propagation analysis in a functionally graded nanocomposite cylinder reinforced by carbon nanotubes (Hosseini 2013, 2014a). Also, the GFD method has been used for various types of engineering problems (Benito *et al*. 2013, Gavete *et al*. 2013, Hosseini 2014b and 2015). Furthermore, the meshless GFD method has been applied to inverse problems such as inverse biharmonic boundary value problems (Fan *et al*. 2014) and Cauchy problem for various kinds of partial differential equations (Fan 2015). Recently, Gu *et al*. (2017) employed the meshless GFD method for solving the inverse heat source problem associated with the steady-state heat conduction.

This paper presents the first attempt for the application of a modified micromechanical model to the elastic wave propagation analysis in a FG graphene platelets-reinforced thick hollow cylinder using the meshless GFD method. The present micromechanical model considers the nonlinear distributions of the GPLs along the radial direction of cylinder. Using the three different nonlinear functions for the volume fraction of the GPLs, various nonlinear grading patterns can be applied for the nonlinear distributions of the GPLs across the thickness of the thick hollow cylinder along the radial direction. The wave propagation characteristics in both the displacement and the stress fields are obtained and discussed in detail.

A modified micromechanical model is proposed to simulate the various nonlinear grading patterns of GPLs distributions in the reinforced nanocomposite structures, which can be considered as one of the originalities and novelties of the present research. In the previous published works, the distributions of GPLs in nanocomposite structures were considered to vary linearly through certain direction in the reinforced structures. Recently, using the linear distributions of GPLs in the FG multilayer reinforced nanocomposite beam, the buckling and postbuckling analysis and nonlinear free vibration were carried out (Feng *et al*. 2017a, Yang *et al*. 2017). The proposed nonlinear micromechanical model in this paper furnishes a ground for considering the nonlinear distributions of GPLs in various engineering analysis of reinforced nanocomposite structures.

Also, the modified micromechanical model, which is proposed in this paper, is successfully employed for elastic wave propagation analysis in the GPLs-reinforced nanocomposite cylinder with various nonlinear grading patterns of GPLs distributions. The governing equations are derived considering the nonlinearity in the GPLs distributions and then solved by developing the meshless GFD method. The effects of various nonlinear grading patterns of GPLs distributions on the elastic wave propagation are obtained and studied in a shock-induced reinforced nanocomposite cylinder.

2. Modified micromechanical model

A thick hollow cylinder with a finite length L, an inner radius r_{in} and an outer radius r_{out} is considered in this analysis, which is reinforced by the GPLs under axisymmetric conditions (see Fig. 1). It is assumed that the GPLs are non-uniformly distributed within the polymer matrix along the radial direction of the cylinder with a nonlinear distribution. Also, it is assumed that the distribution of the GPLs is varied from inner surface of cylinder to outer surface along the radial direction. Hence, the considered cylinder has a functionally graded distribution of the GPLs, which varies nonlinearly along the radial direction.

Based on the Halpin-Tsai micromechanical model, the elastic modulus of the composites with randomly oriented fillers can be approximated by (Yang *et al*. 2017) as

$$E = \frac{3}{8}E_L + \frac{5}{8}E_T \tag{1}$$

where the terms E_L and E_T stand for the longitudinal and transverse moduli for a unidirectional lamina. The terms E_L and E_T can be calculated by the Halpin-Tsai model as (Yang *et al*. 2017)

in

$$E_L = \frac{1+\xi_L\eta_L V_f}{1-\eta_L V_f}E_m \tag{2}$$

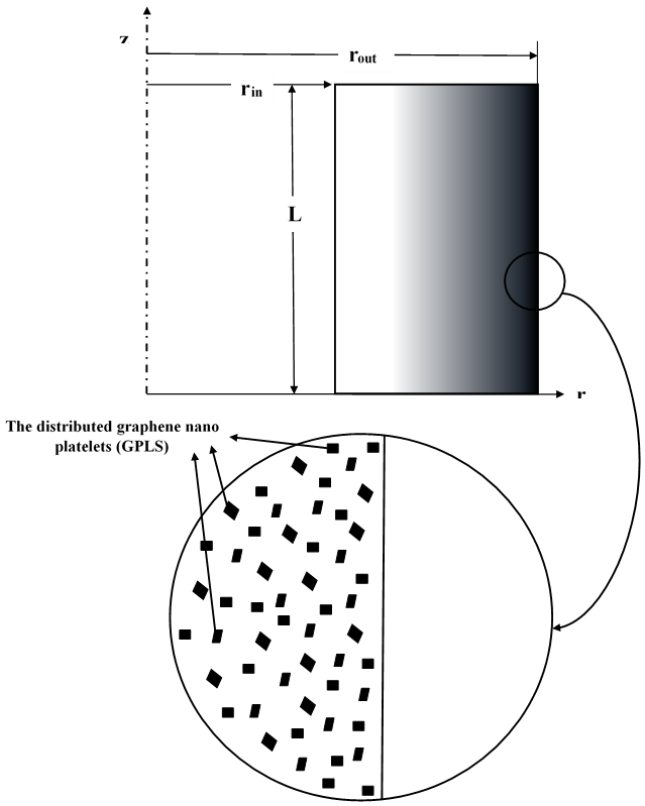

Fig. 1 The sketch of the FGGPLs-reinforced thick hollow cylinder with a finite length

$$E_T = \frac{1+\xi_T \eta_T V_f}{1-\eta_T V_f} E_m \tag{3}$$

where the filler volume fraction is defined by V_f. Eq. (1) can be modified for the considered problem as

$$E(r) = \frac{3}{8} E_L(r) + \frac{5}{8} E_T(r) \tag{4}$$

in which r is the radius of the thick hollow cylinder. So, the longitudinal and transverse moduli determined by Eqs. (2) and (3) can also be written as

$$E_L(r) = \frac{1+\xi_L \eta_L V_{GPL}(r)}{1-\eta_L V_{GPL}(r)} E_m \tag{5}$$

$$E_T(r) = \frac{1+\xi_T \eta_T V_{GPL}(r)}{1-\eta_T V_{GPL}(r)} E_m \tag{6}$$

Thus, we have

$$E(r) = \frac{3}{8}\left[\frac{1+\xi_L \eta_L V_{GPL}(r)}{1-\eta_L V_{GPL}(r)}\right] E_m + \frac{5}{8}\left[\frac{1+\xi_T \eta_T V_{GPL}(r)}{1-\eta_T V_{GPL}(r)}\right] E_m \tag{7}$$

where $V_{GPL}(r)$ is the volume fraction of the GPLs that is dependent on the radius. The terms η_L and η_T can be calculated as (Yang *et al*. 2017)

$$\eta_L = \frac{\left(E_{GPL}/E_m\right)-1}{\left(E_{GPL}/E_m\right)+\xi_L} \tag{8}$$

$$\eta_T = \frac{\left(E_{GPL}/E_m\right)-1}{\left(E_{GPL}/E_m\right)+\xi_T} \tag{9}$$

The modulus of elasticity for the GPL and the matrix is E_{GPL} and E_m, respectively. The terms ξ_L and ξ_T are the geometry factors of the GPLs, which are obtained as (Yang *et al*. 2017)

$$\xi_L = 2\left(a_{GPL}/t_{GPL}\right) \tag{10}$$

$$\xi_T = 2\left(b_{GPL}/t_{GPL}\right) \tag{11}$$

where a_{GPL}, b_{GPL} and t_{GPL} are the length, width and thickness of the GPLs, respectively. To find the GPL volume fraction, it is needed to describe the nonlinear variation of the GPLs distribution.

So, in this work, three types of the nonlinear functions are used for $V_{GPL}(r)$. The three nonlinear functions for $V_{GPL}(r)$ and the first derivative of $V_{GPL}(r)$ with respect to r can be stated as follows:

- Type V

$$V_{GPL}(r) = 2V^*_{GPL}\left(\frac{r-r_{in}}{r_{out}-r_{in}}\right)^n \tag{12}$$

$$V'_{GPL}(r) = \frac{d}{dr}V_{GPL}(r) = 2nV^*_{GPL}\frac{\left(r-r_{in}\right)^{n-1}}{\left(r_{out}-r_{in}\right)^n} \tag{13}$$

- Type Λ

$$V_{GPL}(r) = 2V^*_{GPL}\left(\frac{r_{out}-r}{r_{out}-r_{in}}\right)^n \tag{14}$$

$$V'_{GPL}(r) = \frac{d}{dr}V_{GPL}(r) = -2nV^*_{GPL}\frac{\left(r_{out}-r\right)^{n-1}}{\left(r_{out}-r_{in}\right)^n} \tag{15}$$

- Type X

$$V_{GPL}(r) = 4HV^*_{GPL}\left(\frac{r-r_m}{r_{out}-r_{in}}\right)^n \tag{16}$$

$$r_m = \frac{r_{out} - r_{in}}{2}$$
$$H = \frac{r_{out} - r_{in}}{\left(r_{out} - r_{in}\right)^n} \tag{16}$$

$$V'_{GPL}(r) = \frac{d}{dr} V_{GPL}(r)$$
$$= 4nHV^*_{GPL} \frac{\left(r - r_m\right)^{n-1}}{\left(r_{out} - r_{in}\right)^n} \tag{17}$$

where

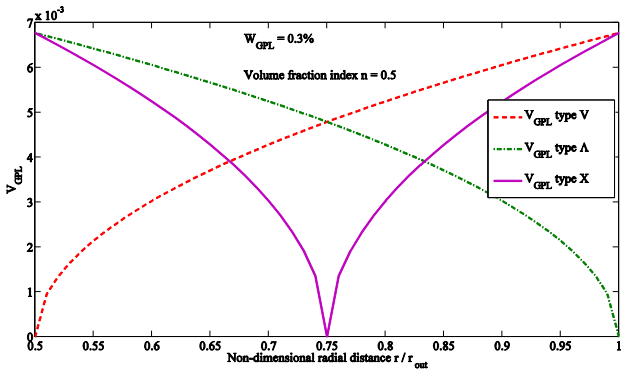

(a)

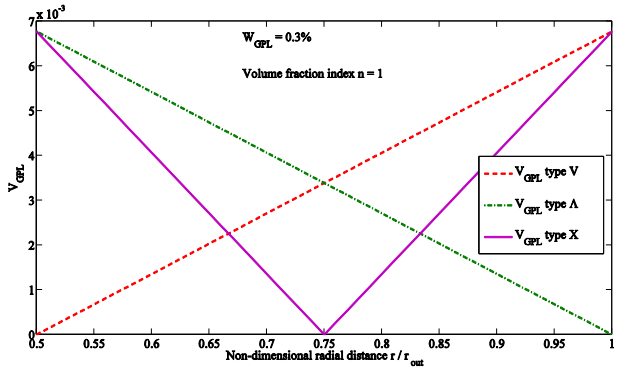

(b)

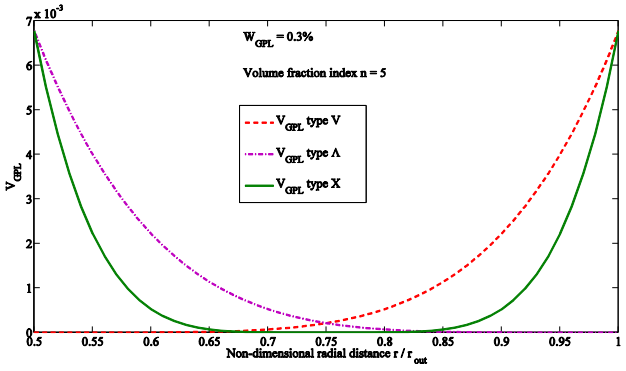

(c)

Fig. 2 The variations of three types of V_{GPL} (r) for various values of the volume fraction index: (a) n < 1; (b) n = 1; (c) n > 1

$$V^*_{GPL} = \frac{W_{GPL}}{W_{GPL} + \left(\rho_{GPL}/\rho_m\right)\left(1 - W_{GPL}\right)} \tag{18}$$

in which W_{GPL} is the GPL weight fraction, and ρ_{GPL} and ρ_m are the mass densities of the GPLs and the polymer matrix, respectively. The variations of the three types of W_{GPL} are demonstrated in Fig. 2 for three values of the volume fraction index. To describe the density $\rho(r)$ and Poisson's ratio $\nu(r)$ of the FGGPLs-reinforced composite thick hollow cylinder, the rule of mixture is used as follows

$$\rho(r) = \rho_{GPL} V_{GPL}(r) + \rho_m V_m(r)$$
$$= \left(\rho_{GPL} - \rho_m\right) V_{GPL}(r) + \rho_m \tag{19}$$

$$\nu(r) = \nu_{GPL} V_{GPL}(r) + \nu_m V_m(r)$$
$$= \left(\nu_{GPL} - \nu_m\right) V_{GPL}(r) + \nu_m \tag{20}$$

$$V_{GPL}(r) + V_m(r) = 1 \tag{21}$$

3. Governing equations

The governing equations for the FGGPLs-reinforced composite thick hollow cylinder with a finite length and an axisymmetric deformation can be written as (see Fig. 1)

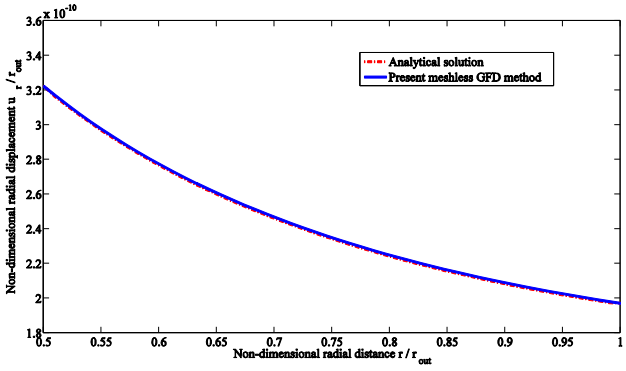

(a)

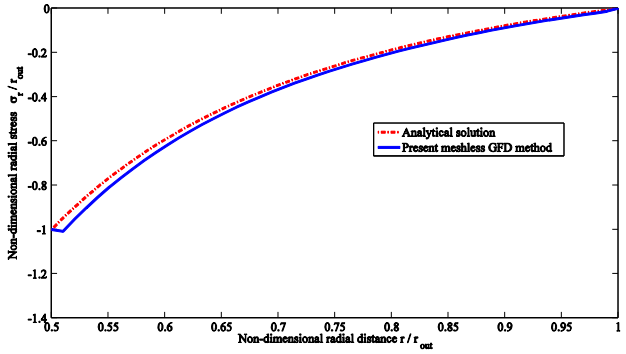

(b)

Fig. 3 The comparisons between the present results and those obtained from analytical solution:
(a) Non-dimensional radial displacement;
(b) Non-dimensional radial stress

$$\frac{\partial\sigma_r(r,z,t)}{\partial r}+\frac{\sigma_r(r,z,t)-\sigma_\theta(r,z,t)}{r}+\frac{\partial\tau_{rz}(r,z,t)}{\partial z}=\rho(r)\frac{\partial^2 u_r(r,z,t)}{\partial t^2} \tag{22}$$

$$\frac{\partial\sigma_z(r,z,t)}{\partial z}+\frac{\partial\tau_{rz}(r,z,t)}{\partial r}+\frac{\tau_{rz}(r,z,t)}{r}=\rho(r)\frac{\partial^2 u_z(r,z,t)}{\partial t^2} \tag{23}$$

where $\sigma_r(r, z, t)$, $\sigma_z(r, z, t)$ and $\sigma_\theta(r, z, t)$ are the radial, axial and hoop stresses, respectively. The terms u_r and u_z stand for the radial and axial displacements. The governing equations can also be rewritten in terms of the displacements as

$$\begin{aligned}&C_1(r)\left(\frac{\partial^2 u_r}{\partial r^2}+\frac{1}{r}\frac{\partial u_r}{\partial r}-\frac{u_r}{r^2}\right)+C_1^{'}(r)\frac{\partial u_r}{\partial r}\\&+C_2(r)\frac{\partial^2 u_z}{\partial r\partial z}+C_2^{'}(r)\frac{u_r}{r}+C_2^{'}(r)\frac{\partial u_z}{\partial z}\\&+G(r)\frac{\partial^2 u_r}{\partial z^2}+G(r)\frac{\partial^2 u_z}{\partial r\partial z}=\rho(r)\frac{\partial^2 u_r}{\partial t^2}\end{aligned} \tag{24}$$

$$\begin{aligned}&C_1(r)\frac{\partial^2 u_z}{\partial z^2}+C_2(r)\frac{\partial^2 u_r}{\partial r\partial z}+C_2(r)\frac{1}{r}\frac{\partial u_r}{\partial z}\\&+G^{'}(r)\frac{\partial u_r}{\partial z}+G(r)\frac{\partial^2 u_r}{\partial r\partial z}+G^{'}(r)\frac{\partial u_z}{\partial r}\\&+G(r)\frac{\partial^2 u_z}{\partial r^2}+G(r)\frac{1}{r}\frac{\partial u_r}{\partial z}\\&+G(r)\frac{1}{r}\frac{\partial u_z}{\partial r}=\rho(r)\frac{\partial^2 u_z}{\partial t^2}\end{aligned} \tag{25}$$

in which the factors $C_1(r)$, $C_2(r)$ and $C(r)$ are given by

$$C_1(r)=\frac{E(r)\left[1-\nu(r)\right]}{\left[1+\nu(r)\right]\left[1-2\nu(r)\right]} \tag{26}$$

$$C_2(r)=\frac{E(r)\nu(r)}{\left[1+\nu(r)\right]\left[1-2\nu(r)\right]} \tag{27}$$

$$G(r)=\frac{E(r)}{2\left[1+\nu(r)\right]} \tag{28}$$

The first derivatives of $G_1(r)$, $G_2(r)$ and $G(r)$ with respect to r are obtained as

$$C_1^{'}(r)=\frac{d}{dr}C_1(r)=\left\{E^{'}(r)\left[1-2\nu(r)-\nu^2(r)+2\nu^3(r)\right]+2E(r)\nu(r)\nu^{'}(r)\left[2-\nu(r)\right]\right\}\Big/\left[1-\nu(r)-2\nu^2(r)\right]^2 \tag{29}$$

$$C_2^{'}(r)=\frac{d}{dr}C_2(r)=\left\{E^{'}(r)\nu(r)\left[1-\nu(r)-2\nu^2(r)\right]+E(r)\nu^{'}(r)\left[1+2\nu^2(r)\right]\right\}\Big/\left[1-\nu(r)-2\nu^2(r)\right]^2 \tag{30}$$

$$\begin{aligned}G^{'}(r)&=\frac{d}{dr}G(r)\\&=\left\{E^{'}(r)\left[1+\nu(r)\right]-E(r)\nu^{'}(r)\right\}\Big/2\left[1+\nu(r)\right]^2\end{aligned} \tag{31}$$

where

$$\begin{aligned}E^{'}(r)&=\frac{d}{dr}E(r)\\&=V_{GPL}^{'}(r)\left\{\frac{3\eta_L\left(1+\xi_L\right)}{8\left[1-\eta_L V_{GPL}(r)\right]^2}+\frac{5\eta_T\left(1+\xi_T\right)}{8\left[1-\eta_T V_{GPL}(r)\right]^2}\right\}\end{aligned} \tag{32}$$

$$\nu^{'}(r)=\frac{d}{dr}\nu(r)=V_{GPL}^{'}(r)\left(\nu_{GPL}-\nu_m\right) \tag{33}$$

The first derivative of the GPLs volume fraction with respect to the radius $V'_{GPL}(r)$ can be calculated by using Eqs. (13), (15) and (17).

4. Meshless generalized finite difference (GFD) method

4.1 General formulations

In the GFD method, the partial derivatives of the field quantities are linearly approximated by the Taylor-series expansion on some nodes (center nodes) in the analyzed domain, where each center node is surrounded by some other nodes. The nodes can be regularly or randomly distributed in the analyzed domain. Consequently, the partial derivatives are obtained at the rest of the center nodes, and the group of nodes with a center node and other surrounding nodes is called a star in this method.

For differentiable displacement functions $u_r = u_r(r, z, t)$ and $u_z = u_z(r, z, t)$ in a 2D domain, the Taylor-series expansion around an arbitrary point (r_0, z_0, t) can be expressed as follows

$$\begin{aligned}u_r^i&=u_r^0+h_i\frac{\partial u_r^0}{\partial r}+k_i\frac{\partial u_r^0}{\partial z}+\frac{{h_i}^2}{2}\frac{\partial^2 u_r^0}{\partial r^2}\\&+\frac{{k_i}^2}{2}\frac{\partial^2 u_r^0}{\partial z^2}+h_i k_i\frac{\partial^2 u_r^0}{\partial r\,\partial z}u_r^0+o\left(\tilde{r}_i^{\,3}\right)\end{aligned} \tag{34}$$

$$u_z^i=u_z^0+h_i\frac{\partial u_z^0}{\partial r}+k_i\frac{\partial u_z^0}{\partial z}+\frac{{h_i}^2}{2}\frac{\partial^2 u_z^0}{\partial r^2} \tag{35}$$

$$+\frac{k_i^2}{2}\frac{\partial^2 u_z^0}{\partial z^2}+h_i k_i\frac{\partial^2 u_z^0}{\partial r\partial z}+o\left(\tilde{r}_i^3\right) \tag{35}$$

where $u_r^0 = u_r(r_0, z_0, t)$, $u_z^0 = u_z(r_0, z_0, t)$, $h_i = r_i - r_0$, $k_i = z_i - z_0$ and $\tilde{r}_i = \sqrt{h_i^2 + k_i^2}$.

$$B_r^u = \sum_{i=1}^{N}\left[\left(u_r^0 - u_r^i + h_i\frac{\partial u_r^0}{\partial r} + k_i\frac{\partial u_r^0}{\partial z} + \frac{h_i^2}{2}\frac{\partial^2 u_r^0}{\partial r^2} + \frac{k_i^2}{2}\frac{\partial^2 u_r^0}{\partial z^2} + h_i k_i\frac{\partial^2 u_r^0}{\partial r\partial z}\right)w_i\left(h_i,k_i\right)\right]^2 \tag{36}$$

$$B_z^u = \sum_{i=1}^{N}\left[\left(u_z^0 - u_z^i + h_i\frac{\partial u_z^0}{\partial r} + k_i\frac{\partial u_z^0}{\partial z} + \frac{h_i^2}{2}\frac{\partial^2 u_z^0}{\partial r^2} + \frac{k_i^2}{2}\frac{\partial^2 u_z^0}{\partial z^2} + h_i k_i\frac{\partial^2 u_z^0}{\partial r\partial z}\right)w_i\left(h_i,k_i\right)\right]^2 \tag{37}$$

Eqs. (34) and (35) are limited to the second-order approximations and two-dimensional cases, which are assumed in the present analysis. It is also possible to develop the extensions of the formulation to 3D problems. The norm functions B_r^u and B_z^u can be defined in the following forms:

where $w_i(h_i, k_i)$ is the weight function, and N stands for the number of nearest nodes surround the central node (r_0, z_0, t) in each star. In this paper, the weight function is defined by

$$w_i\left(h_i,k_i\right) = \frac{1}{\left(\sqrt{h_i^2+k_i^2}\right)^3} = \left(h_i^2+k_i^2\right)^{-\frac{3}{2}} \tag{38}$$

By minimizing the norms B_r^u and B_z^u with respect to the partial derivatives, the following linear equations can be derived

$$\frac{\partial B_r^u}{\partial\left\{Du_r^0\right\}} = 0 \tag{39}$$

$$\left\{Du_r^0\right\}^T = \left\{\frac{\partial u_r^0}{\partial r}, \frac{\partial u_r^0}{\partial z}, \frac{\partial^2 u_r^0}{\partial r^2}, \frac{\partial^2 u_r^0}{\partial z^2}, \frac{\partial^2 u_r^0}{\partial r\partial z}\right\}^T \tag{40}$$

$$\frac{\partial B_z^u}{\partial\left\{Du_z^0\right\}} = 0 \tag{41}$$

$$\left\{Du_z^0\right\}^T = \left\{\frac{\partial u_z^0}{\partial r}, \frac{\partial u_z^0}{\partial z}, \frac{\partial^2 u_z^0}{\partial r^2}, \frac{\partial^2 u_z^0}{\partial z^2}, \frac{\partial^2 u_z^0}{\partial r\partial z}\right\}^T \tag{42}$$

In the following, the solution procedures for u_r^0 are developed, and the similar procedures can be applied for u_z^0. For each node, the five equations can be obtained for the five unknowns as follows

$$\begin{aligned}&\frac{\partial u_r^0}{\partial r}\sum_{i=1}^{N} w_i^2 h_i^2 + \frac{\partial u_r^0}{\partial z}\sum_{i=1}^{N} w_i^2 h_i k_i \\ &+\frac{\partial^2 u_r^0}{\partial r^2}\sum_{i=1}^{N} w_i^2\frac{h_i^3}{2} + \frac{\partial^2 u_r^0}{\partial z^2}\sum_{i=1}^{N} w_i^2\frac{h_i k_i^2}{2} \\ &+\frac{\partial^2 u_r^0}{\partial z\partial r}\sum_{i=1}^{N} w_i^2 h_i^2 k_i + u_r^0\sum_{i=1}^{N} w_i^2 h_i \\ &-\sum_{i=1}^{N} w_i^2 h_i u_r^i = 0,\end{aligned} \tag{43}$$

$$\begin{aligned}&\frac{\partial u_r^0}{\partial r}\sum_{i=1}^{N} w_i^2 h_i k_i + \frac{\partial u_r^0}{\partial z}\sum_{i=1}^{N} w_i^2 k_i^2 \\ &+\frac{\partial^2 u_r^0}{\partial r^2}\sum_{i=1}^{N} w_i^2\frac{h_i^2 k_i}{2} + \frac{\partial^2 u_r^0}{\partial z^2}\sum_{i=1}^{N} w_i^2\frac{k_i^3}{2} \\ &+\frac{\partial^2 u_r^0}{\partial z\partial r}\sum_{i=1}^{N} w_i^2 h_i k_i^2 + u_r^0\sum_{i=1}^{N} w_i^2 k_i \\ &-\sum_{i=1}^{N} w_i^2 k_i u_r^i = 0,\end{aligned} \tag{44}$$

$$\begin{aligned}&\frac{\partial u_r^0}{\partial r}\sum_{i=1}^{N} w_i^2\frac{h_i^3}{2} + \frac{\partial u_r^0}{\partial z}\sum_{i=1}^{N} w_i^2\frac{h_i^2 k_i}{2} \\ &+\frac{\partial^2 u_r^0}{\partial r^2}\sum_{i=1}^{N} w_i^2\frac{h_i^4}{4} + \frac{\partial^2 u_r^0}{\partial z^2}\sum_{i=1}^{N} w_i^2\frac{k_i^2 h_i^2}{4} \\ &+\frac{\partial^2 u_r^0}{\partial z\partial r}\sum_{i=1}^{N} w_i^2\frac{h_i^3 k_i}{2} + u_r^0\sum_{i=1}^{N} w_i^2\frac{h_i^2}{2} \\ &-\sum_{i=1}^{N} w_i^2\frac{h_i^2}{2}u_r^i = 0,\end{aligned} \tag{45}$$

$$\begin{aligned}&\frac{\partial u_r^0}{\partial r}\sum_{i=1}^{N} w_i^2\frac{h_i k_i^2}{2} + \frac{\partial u_r^0}{\partial z}\sum_{i=1}^{N} w_i^2\frac{k_i^3}{2} \\ &+\frac{\partial^2 u_r^0}{\partial r^2}\sum_{i=1}^{N} w_i^2\frac{h_i^2 k_i^2}{4} + \frac{\partial^2 u_r^0}{\partial z^2}\sum_{i=1}^{N} w_i^2\frac{k_i^4}{4} \\ &+\frac{\partial^2 u_r^0}{\partial z\partial r}\sum_{i=1}^{N} w_i^2\frac{h_i k_i^3}{2} + u_r^0\sum_{i=1}^{N} w_i^2\frac{k_i^2}{2} \\ &-\sum_{i=1}^{N} w_i^2\frac{k_i^2}{2}u_r^i = 0,\end{aligned} \tag{46}$$

$$\begin{aligned}&\frac{\partial u_r^0}{\partial r}\sum_{i=1}^{N} w_i{}^2 h_i{}^2 k_i+\frac{\partial u_r^0}{\partial z}\sum_{i=1}^{N} w_i{}^2 h_i k_i{}^2\\&+\frac{\partial^2 u_r^0}{\partial r^2}\sum_{i=1}^{N} w_i{}^2\frac{h_i{}^3 k_i}{2}+\frac{\partial^2 u_r^0}{\partial z^2}\sum_{i=1}^{N} w_i{}^2\frac{h_i k_i{}^3}{2}\\&+\frac{\partial^2 u_r^0}{\partial z\partial r}\sum_{i=1}^{N} w_i{}^2 h_i{}^2 k_i{}^2+u_r^0\sum_{i=1}^{N} w_i{}^2 h_i k_i\\&-\sum_{i=1}^{N} w_i{}^2 h_i k_i u_r^i=0.\end{aligned}\tag{47}$$

The above equations can be given in the matrix form as

$$\mathbf{A}^{*}\,\mathbf{D}_{\mathbf{r}}^{\mathbf{u}}=\mathbf{F}_{\mathbf{r}}^{\mathbf{u}}\tag{48}$$

where

$$\mathbf{D}_{\mathbf{r}}^{\mathbf{u}}=\left\{\frac{\partial u_r^0}{\partial r},\frac{\partial u_r^0}{\partial z},\frac{\partial^2 u_r^0}{\partial r^2},\frac{\partial^2 u_r^0}{\partial z^2},\frac{\partial^2 u_r^0}{\partial z\partial r}\right\}^{T}\tag{49}$$

$$\mathbf{F}_{\mathbf{r}}^{\mathbf{u}}=\begin{bmatrix}-u_r^0\sum_{i=1}^{N} w_i{}^2 h_i+\sum_{i=1}^{N} w_i{}^2 h_i u_r^i\\-u_r^0\sum_{i=1}^{N} w_i{}^2 k_i+\sum_{i=1}^{N} w_i{}^2 k_i u_r^i\\-u_r^0\sum_{i=1}^{N} w_i{}^2\frac{h_i{}^2}{2}+\sum_{i=1}^{N} w_i{}^2\frac{h_i{}^2}{2}u_r^i\\-u_r^0\sum_{i=1}^{N} w_i{}^2\frac{k_i{}^2}{2}+\sum_{i=1}^{N} w_i{}^2\frac{k_i{}^2}{2}u_r^i\\-u_r^0\sum_{i=1}^{N} w_i{}^2 h_i k_i+\sum_{i=1}^{N} w_i{}^2 h_i k_i u_r^i\end{bmatrix}\tag{50}$$

$$\mathbf{A}^{*}=\begin{bmatrix}\sum_{i=1}^{N} w_i{}^2 h_i{}^2 & \sum_{i=1}^{N} w_i{}^2 h_i k_i & \sum_{i=1}^{N} w_i{}^2\frac{h_i{}^3}{2} & \sum_{i=1}^{N} w_i{}^2\frac{h_i k_i{}^2}{2} & \sum_{i=1}^{N} w_i{}^2 h_i{}^2 k_i\\\sum_{i=1}^{N} w_i{}^2 h_i k_i & \sum_{i=1}^{N} w_i{}^2 k_i{}^2 & \sum_{i=1}^{N} w_i{}^2\frac{h_i{}^2 k_i}{2} & \sum_{i=1}^{N} w_i{}^2\frac{k_i{}^3}{2} & \sum_{i=1}^{N} w_i{}^2 h_i k_i{}^2\\\sum_{i=1}^{N} w_i{}^2\frac{h_i{}^3}{2} & \sum_{i=1}^{N} w_i{}^2\frac{h_i{}^2 k_i}{2} & \sum_{i=1}^{N} w_i{}^2\frac{h_i{}^4}{4} & \sum_{i=1}^{N} w_i{}^2\frac{k_i{}^2 h_i{}^2}{4} & \sum_{i=1}^{N} w_i{}^2\frac{h_i{}^3 k_i}{2}\\\sum_{i=1}^{N} w_i{}^2\frac{h_i k_i{}^2}{2} & \sum_{i=1}^{N} w_i{}^2\frac{k_i{}^3}{2} & \sum_{i=1}^{N} w_i{}^2\frac{h_i{}^2 k_i{}^2}{4} & \sum_{i=1}^{N} w_i{}^2\frac{k_i{}^4}{4} & \sum_{i=1}^{N} w_i{}^2\frac{h_i k_i{}^3}{2}\\\sum_{i=1}^{N} w_i{}^2 h_i{}^2 k_i & \sum_{i=1}^{N} w_i{}^2 h_i k_i{}^2 & \sum_{i=1}^{N} w_i{}^2\frac{h_i{}^3 k_i}{2} & \sum_{i=1}^{N} w_i{}^2\frac{h_i k_i{}^3}{2} & \sum_{i=1}^{N} w_i{}^2 h_i{}^2 k_i{}^2\end{bmatrix}\tag{51}$$

The solution of Eq. (48) can be given as

$$\mathbf{D}_{\mathbf{r}}^{\mathbf{u}}=\left[\mathbf{A}^{*}\right]^{-1}\mathbf{F}_{\mathbf{r}}^{\mathbf{u}}=\mathbf{B}\,\mathbf{F}_{\mathbf{r}}^{\mathbf{u}}\tag{52}$$

The derivative of u_r^0 can be written in the following form

$$\begin{aligned}\frac{\partial u_r^0}{\partial r}&=B_{11}\left(-u_r^0\sum_{i=1}^{N} w_i{}^2 h_i+\sum_{i=1}^{N} w_i{}^2 h_i u_r^i\right)\\&+B_{12}\left(-u_r^0\sum_{i=1}^{N} w_i{}^2 k_i+\sum_{i=1}^{N} w_i{}^2 k_i u_r^i\right)\\&+B_{13}\left(-u_r^0\sum_{i=1}^{N} w_i{}^2\frac{h_i{}^2}{2}+\sum_{i=1}^{N} w_i{}^2\frac{h_i{}^2}{2}u_r^i\right)\\&+B_{14}\left(-u_r^0\sum_{i=1}^{N} w_i{}^2\frac{k_i{}^2}{2}+\sum_{i=1}^{N} w_i{}^2\frac{k_i{}^2}{2}u_r^i\right)\\&+B_{15}\left(-u_r^0\sum_{i=1}^{N} w_i{}^2 h_i k_i+\sum_{i=1}^{N} w_i{}^2 h_i k_i u_r^i\right)\end{aligned}\tag{53}$$

or

$$\frac{\partial u_r^0}{\partial r}=-u_r^0\,\eta_0+\sum_{i=1}^{N}\eta_i u_r^i\tag{54}$$

where

$$\begin{aligned}\eta_i&=B_{11} w_i{}^2 h_i+B_{12} w_i{}^2 k_i\\&+B_{13} w_i{}^2\frac{h_i{}^2}{2}+B_{14} w_i{}^2\frac{k_i{}^2}{2}+B_{15} w_i{}^2 h_i k_i\end{aligned}\tag{55}$$

and

$$\eta_0=\sum_{i=1}^{N}\eta_i\tag{56}$$

By using the similar way, other derivatives of u_r^0 can be obtained as

$$\frac{\partial u_r^0}{\partial z}=-u_r^0\,\lambda_0+\sum_{i=1}^{N}\lambda_i u_r^i\tag{57}$$

$$\begin{aligned}\lambda_i&=B_{21} w_i{}^2 h_i+B_{22} w_i{}^2 k_i\\&+B_{23} w_i{}^2\frac{h_i{}^2}{2}+B_{24} w_i{}^2\frac{k_i{}^2}{2}+B_{25} w_i{}^2 h_i k_i\end{aligned}\tag{58}$$

$$\lambda_0=\sum_{i=1}^{N}\lambda_i\tag{59}$$

and

$$\frac{\partial^2 u_r^0}{\partial r^2}=-u_r^0\,\tau_0+\sum_{i=1}^{N}\tau_i u_r^i\tag{60}$$

$$\begin{aligned}\tau_i&=B_{31} w_i{}^2 h_i+B_{32} w_i{}^2 k_i\\&+B_{33} w_i{}^2\frac{h_i{}^2}{2}+B_{34} w_i{}^2\frac{k_i{}^2}{2}+B_{35} w_i{}^2 h_i k_i\end{aligned}\tag{61}$$

$$\tau_0 = \sum_{i=1}^{N} \tau_i \tag{62}$$

and

$$\frac{\partial^2 u_r^0}{\partial z^2} = -u_r^0 \psi_0 + \sum_{i=1}^{N} \psi_i u_r^i \tag{63}$$

$$\begin{aligned} \psi_i &= B_{41} w_i^{\,2} h_i + B_{42} w_i^{\,2} k_i \\ &+ B_{43} w_i^{\,2} \frac{h_i^{\,2}}{2} + B_{44} w_i^{\,2} \frac{k_i^{\,2}}{2} + B_{45} w_i^{\,2} h_i k_i \end{aligned} \tag{64}$$

$$\psi_0 = \sum_{i=1}^{N} \psi_i \tag{65}$$

and also

$$\frac{\partial^2 u_r^0}{\partial z \partial r} = -u_r^0 \varphi_0 + \sum_{i=1}^{N} \varphi_i u_r^i \tag{66}$$

$$\begin{aligned} \varphi_i &= B_{51} w_i^{\,2} h_i + B_{52} w_i^{\,2} k_i \\ &+ B_{53} w_i^{\,2} \frac{h_i^{\,2}}{2} + B_{54} w_i^{\,2} \frac{k_i^{\,2}}{2} + B_{55} w_i^{\,2} h_i k_i \end{aligned} \tag{67}$$

$$\varphi_0 = \sum_{i=1}^{N} \varphi_i \tag{68}$$

The terms B_{ij} are the components of the matrix **B**. The derivatives of u_z^0 can be obtained by employing the similar procedures as

$$\frac{\partial u_z^0}{\partial r} = -\eta_0 u_z^0 + \sum_{i=1}^{N} \eta_i u_z^i \tag{69}$$

$$\frac{\partial u_z^0}{\partial z} = -\lambda_0 u_z^0 + \sum_{i=1}^{N} \lambda_i u_z^i \tag{70}$$

$$\frac{\partial^2 u_z^0}{\partial r^2} = -\tau_0 u_z^0 + \sum_{i=1}^{N} \tau_i u_z^i \tag{71}$$

$$\frac{\partial^2 u_z^0}{\partial z^2} = -\psi_0 u_z^0 + \sum_{i=1}^{N} \psi_i u_z^i \tag{72}$$

$$\frac{\partial^2 u_z^0}{\partial r \partial z} = -\varphi_0 u_z^0 + \sum_{i=1}^{N} \varphi_i u_z^i \tag{73}$$

The above obtained equations for the derivatives of u_r^0 and u_z^0 are the so called star forms. By substituting the obtained relations in star forms for the derivatives of the displacements into the governing Eqs. (24) and (25) at an arbitrary center node (r_0, z_0, t), the governing equations can be obtained in the discretized forms for the GFD method, which will be presented in the following.

4.2 The discretized governing equations in the GFD method

By substituting the first and second derivatives of the displacements into the Eqs. (24) and (25), the discretized forms of the governing equations can be written for an arbitrary center point (r_0, z_0, t) as

$$\begin{aligned} &C_1(r_0)\left(-u_r^0 \tau_0 + \sum_{i=1}^{N} \tau_i u_r^i\right) \\ &+C_1(r_0)\frac{1}{r_0}\left(-u_r^0 \eta_0 + \sum_{i=1}^{N} \eta_i u_r^i\right) \\ &+C_1^{'}(r_0)\left(-u_r^0 \eta_0 + \sum_{i=1}^{N} \eta_i u_r^i\right) \\ &+C_2(r_0)\left(-u_z^0 \varphi_0 + \sum_{i=1}^{N} \varphi_i u_z^i\right) \\ &+C_2^{'}(r_0)\left(-\lambda_0 u_z^0 + \sum_{i=1}^{N} \lambda_i u_z^i\right) \\ &+G(r_0)\left(-u_r^0 \psi_0 + \sum_{i=1}^{N} \psi_i u_r^i\right) \\ &+G(r_0)\left(-\varphi_0 u_z^0 + \sum_{i=1}^{N} \varphi_i u_z^i\right) \\ &-C_1(r_0)\frac{u_r^0}{r_0^{\,2}} + C_2^{'}(r_0)\frac{u_r^0}{r_0} = \rho(r_0)\frac{\partial^2 u_r^0}{\partial t^2}, \end{aligned} \tag{74}$$

$$\begin{aligned} &C_1(r_0)\left(-\psi_0 u_z^0 + \sum_{i=1}^{N} \psi_i u_z^i\right) \\ &+C_2(r_0)\left(-u_r^0 \varphi_0 + \sum_{i=1}^{N} \varphi_i u_r^i\right) \\ &+C_2(r_0)\frac{1}{r_0}\left(-\lambda_0 u_r^0 + \sum_{i=1}^{N} \lambda_i u_r^i\right) \\ &+G^{'}(r_0)\left(-u_r^0 \lambda_0 + \sum_{i=1}^{N} \lambda_i u_r^i\right) \\ &+G(r_0)\left(-u_r^0 \varphi_0 + \sum_{i=1}^{N} \varphi_i u_r^i\right) \\ &+G^{'}(r_0)\left(-\eta_0 u_z^0 + \sum_{i=1}^{N} \eta_i u_z^i\right) \end{aligned} \tag{75}$$

$$
\begin{aligned}
&+G(r_0)\left(-\tau_0 u_z^0+\sum_{i=1}^{N}\tau_i u_z^i\right)\\
&+G(r_0)\frac{1}{r_0}\left(-u_r^0\lambda_0+\sum_{i=1}^{N}\lambda_i u_r^i\right)\\
&+G(r_0)\frac{1}{r_0}\left(-\eta_0 u_z^0+\sum_{i=1}^{N}\eta_i u_z^i\right)\\
&=\rho(r_0)\frac{\partial^2 u_z^0}{\partial t^2}.
\end{aligned}
\tag{75}
$$

$$
\begin{aligned}
&-\left\{C_1(r_0)\tau_0+C_1(r_0)\frac{1}{r_0}\eta_0+C_1^{'}(r_0)\eta_0\right.\\
&\quad\left.+G(r_0)\psi_0+C_1(r_0)\frac{1}{{r_0}^2}-C_2^{'}(r_0)\frac{1}{r_0}\right\}u_r^0\\
&+\sum_{i=1}^{N}\left\{C_1(r_0)\tau_i+C_1(r_0)\frac{1}{r_0}\eta_i\right.\\
&\quad\left.+C_1^{'}(r_0)\eta_i+G(r_0)\psi_i\right\}u_r^i\\
&-\left\{C_2(r_0)\varphi_0+C_2^{'}(r_0)\lambda_0+G(r_0)\varphi_0\right\}u_z^0\\
&+\sum_{i=1}^{N}\left\{C_2(r_0)\varphi_i+C_2^{'}(r_0)\lambda_i+G(r_0)\varphi_i\right\}u_z^i\\
&=\rho(r_0)\frac{\partial^2 u_r^0}{\partial t^2},
\end{aligned}
\tag{76}
$$

$$
\begin{aligned}
&-\left\{C_2(r_0)\varphi_0+C_2(r_0)\frac{1}{r_0}\lambda_0+G^{'}(r_0)\lambda_0\right.\\
&\left.+G(r_0)\varphi_0+G(r_0)\frac{1}{r_0}\lambda_0\right\}u_r^0\\
&+\sum_{i=1}^{N}\left\{C_2(r_0)\varphi_i+C_2(r_0)\frac{1}{r_0}\lambda_i\right.\\
&\left.+G^{'}(r_0)\lambda_i+G(r_0)\varphi_i+G(r_0)\frac{1}{r_0}\lambda_i\right\}u_r^i\\
&-\left\{C_1(r_0)\psi_0+G^{'}(r_0)\eta_0+G(r_0)\tau_0+G(r_0)\frac{1}{r_0}\eta_0\right\}u_z^0\\
&+\sum_{i=1}^{N}\left\{C_1(r_0)\psi_i+G^{'}(r_0)\eta_i+G(r_0)\tau_i+G(r_0)\frac{1}{r_0}\eta_i\right\}u_z^i\\
&=\rho(r_0)\frac{\partial^2 u_z^0}{\partial t^2}.
\end{aligned}
\tag{77}
$$

The above equations can be rewritten as:

The following system of linear equations is obtained for the distributed nodes on the analyzed domain

$$
\begin{aligned}
&\left[M\right]_{(N+1)*(N+1)}\left\{\ddot{\phi}\right\}_{(N+1)*1}\\
&+\left[K\right]_{(N+1)*(N+1)}\left\{\phi\right\}_{(N+1)*1}=\left[f\right]_{(N+1)*1}
\end{aligned}
\tag{78}
$$

where

$$
\begin{aligned}
\left\{\phi\right\}=\{&u_r^0\quad u_z^0\quad u_r^1\quad u_z^1\quad u_r^2\quad u_z^2\\
&\ldots.\quad \ldots.\qquad u_r^N\quad u_z^N\}^T,
\end{aligned}
\tag{79}
$$

$$
\begin{aligned}
\left\{\ddot{\phi}\right\}=\{&\ddot{u}_r^0\quad \ddot{u}_z^0\quad \ddot{u}_r^1\quad \ddot{u}_z^1\quad \ddot{u}_r^2\quad \ddot{u}_z^2\\
&\ldots.\quad \ldots.\qquad \ddot{u}_r^N\quad \ddot{u}_z^N\}^T.
\end{aligned}
\tag{80}
$$

The double-dot super scripts stand for the second derivatives of the field variables with respect to time.

The components of the matrix $[f]_{(N+1)\times 1}$ are determined by employing the boundary conditions of the considered problem. The unknown nodal values of the field variables in Eq. (78) can be solved by using a proper numerical method. In this paper, the Newmark finite difference method is employed to solve the Eq. (78). Also, it is possible to solve the Eq. (78) using other methods such as the Laplace-transform technique.

5. Numerical results and discussions

We consider a FGGPLs-reinforced thick hollow cylinder made of a mixture of the epoxy and GPLs, which are distributed with various nonlinear grading patterns. The length, width and thickness of the GPLs are assumed to be a_{GPL} = 2.5 μm, b_{GPL} = 1.5 μm and t_{GPL} = 1.5 nm, respectively (Yang *et al*. 2017). The material properties including the elastic modulus, mass density and Poisson's ratio of the epoxy matrix are assumed to be E_m = 3.0 GPa, ρ_m = 1200 kg/m^3 and v_m = 0.34, respectively (Yang *et al*. 2017). The material properties of the GPLs are E_{GPL} = 1.01 TPa, ρ_{GPL} = 1062.5 kg/m^3 and v_{GPL} = 0.186, as reported Yang *et al*. (2017). The boundary conditions of the considered FGGPLs-reinforced thick hollow cylinder, which is shown in Fig. 1, can be formulated as follows

$$\sigma_r\left(r_{in},z,t\right)=F(t),\qquad \tau_{rz}\left(r_{in},z,t\right)=0, \tag{81}$$

$$\sigma_r\left(r_{out},z,t\right)=0,\qquad \tau_{rz}\left(r_{out},z,t\right)=0, \tag{82}$$

$$u_z\left(r,0,t\right)=0,\qquad \tau_{rz}\left(r,0,t\right)=0, \tag{83}$$

$$u_z\left(r,L,t\right)=0,\qquad \tau_{rz}\left(r,L,t\right)=0. \tag{84}$$

To verify the present method and results, it is assumed that the volume fraction index of the GPLs takes a big value such as n = 1000. It means that the thick hollow cylinder is made of a fully isotropic polymer. Also, it is assumed that the hollow cylinder is very long (plane-strain condition) with an axisymmetric deformation. The loading function

$F(t)$ is taken as

$$F(t)=\sigma_0\left(1-e^{-ct}\right) \tag{85}$$

where it is assumed that $\sigma_0 = -E_m = -3.1\times10^{-9}$ Pa or $\sigma_0 = E_m = -1$ and $c = 100$. In the long-time limit, the inside pressure of the thick hollow cylinder converges to a hydrostatic pressure equal to σ_0. Then, it is possible to compare the obtained results in the long-time limit with those obtained from the static analysis of an isotropic hollow cylinder under an internal hydrostatic pressure. The analytical solution for the radial stress and radial displacement of an isotropic hollow cylinder under internal hydrostatic loading are given by (Vullo 2014)

$$\sigma_r=\frac{\sigma_0}{\left(\frac{1}{r_{in}^2}-\frac{1}{r_{out}^2}\right)}\left(\frac{1}{r^2}-1\right) \tag{86}$$

$$u_r=\sigma_0\left(\frac{1}{r_{in}^2}-\frac{1}{r_{out}^2}\right)\left(\frac{1}{r\left(C_2-C_1\right)}-\frac{r}{\left(C_2+C_1\right)}\right) \tag{87}$$

The constants C_1 and C_2 can be obtained as

$$C_1=\frac{E\left(1-\nu\right)}{\left(1+\nu\right)\left(1-2\nu\right)},\qquad C_2=\frac{E\nu}{\left(1+\nu\right)\left(1-2\nu\right)} \tag{88}$$

A good agreement can be found in Figs. 3(a) and (b) by the comparisons between the obtained non-dimensional radial displacement and radial stress in long times and those obtained from the analytical solutions (86) and (87). In order to evaluate the performance of the present method in this example, the following error norm is defined as

$$Err_j=Err(r_j,t)=\left|\frac{u^{analytical}(r_j)-u^{GFD}(r_j,t)}{u^{analytical}(r_j)}\right|*100 \tag{89}$$

The effects of the total node number on the error norm for three values of the radius of the cylinder (j = 1, 2, 3) are illustrated in Fig. 4. It can be seen that when the node number is increased the value of the error norm is decreased and converged to a constant value. It illustrates that the increase of the total node number doesn't affect the numerical results significantly when the number of the nodes is larger than 100.

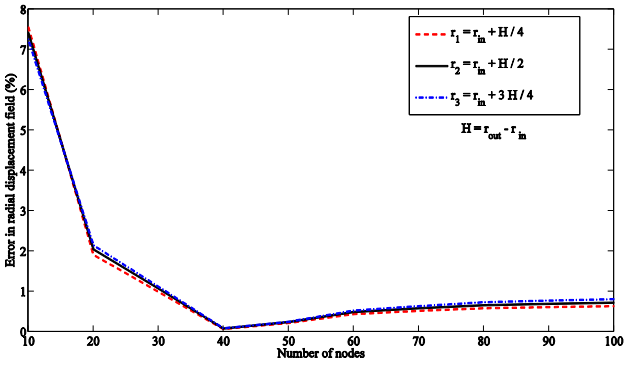

Fig. 4 The effects of the total node number on the error norm for three different radii of the cylinder

As another verification of the present method and results, we consider a cylinder which is made of aluminum (E_m = 70 GPa, ρ_m = 2707 kg/m^3, ν_m = 0.3). By choosing a big value for the volume fraction index n, the mechanical properties of the cylinder approach the properties of the matrix. To compare the obtained results using the present meshless GFD method with those obtained from FEM (Hosseini *et al.* 2007), the following mechanical shock loading is considered for the problem

$$\frac{\sigma_r\left(r_{in},z,t\right)}{E_m}=\begin{cases}0, & t<0,\\ 1, & t\geq 0.\end{cases} \tag{90}$$

Figs. 5-7 show the comparisons between the obtained time histories of the non-dimensional radial displacement, radial and hoop stresses, respectively, with those obtained from FEM. The good agreements can be found in Figs. 5-7.

In order to show the performance of the present GFD method, the following error norm is defined for the non-dimensional radial stress field as

$$Err_j=Err(r,t_j)=\left|\frac{\sigma_r^{FEM}(r,t_j)-\sigma_r^{GFD}(r,t_j)}{\sigma_r^{FEM}(r,t_j)}\right|*100 \tag{91}$$

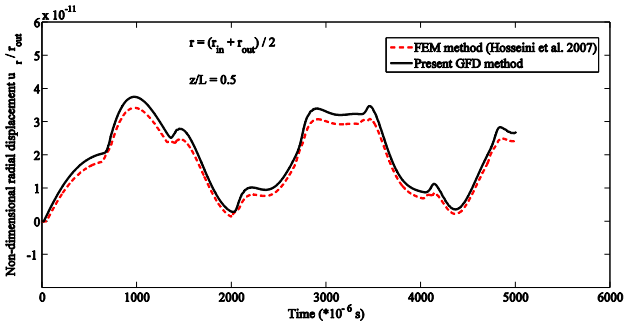

Fig. 5 The comparison between the non-dimensional radial displacements obtained from the GFD method with those obtained from FEM

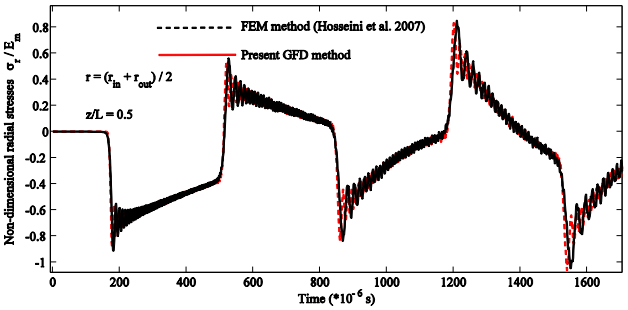

Fig. 6 The comparison between the non-dimensional radial stresses obtained from the GFD method with those obtained from FEM

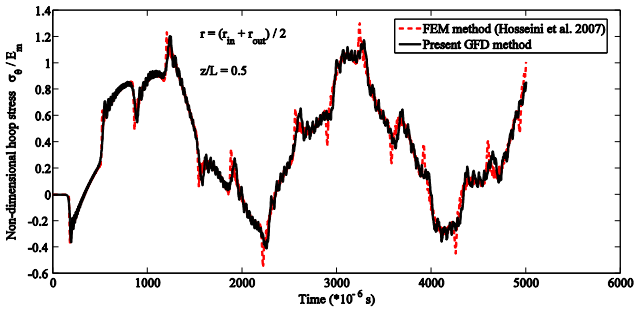

Fig. 7 The comparison between the non-dimensional hoop stresses obtained from the GFD method with those obtained from FEM

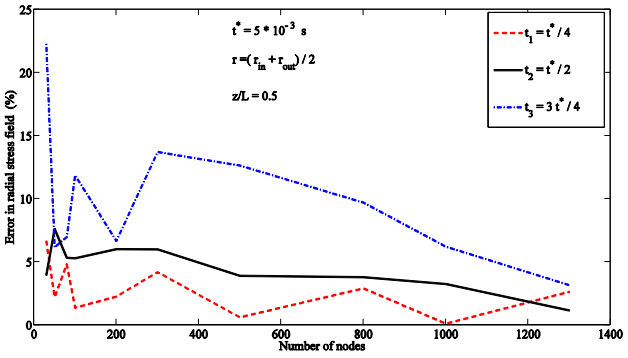

Fig. 8 The effects of the total node number on the error norm at three time instants for the middle point of the thickness of the cylinder

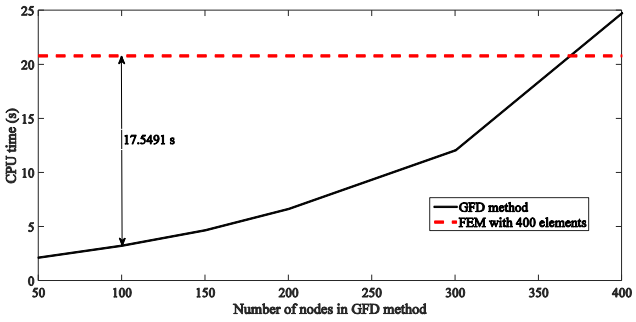

Fig. 9 The effect of total number of nodes on the CPU time of GFD method

The effects of the total node number on the error norm are shown in Fig. 8 for three time instants (j = 1, 2, 3) for the middle point of the thickness of the cylinder ($r = r_m = (r_{out} - r_{in}) / 2$). It can be seen that when the total node is increased the value of the numerical error is decreased to less than 4%. To show the calculation efficiency of the presented meshless GFD method, the CPU time of meshless GFD method is compared to the CPU time of FEM presented by Hosseini *et al*. (2007). Both codes were run by the same PC and software. It is obtained that the CPU time of GFD code is about 3.2576s with considering the total number of nodes to be equal to 100 and the CPU time of FEM is about 20.8067s with considering 400 elements. It means that the CPU time of GFD code is much less than the CPU time of FEM with the acceptable numerical error, which was discussed in Fig. 8. Also, the effect of total number of nodes in GFD method on the CPU time is shown in Fig. 9. It can be clearly observed that the CPU time of GFD method is increased by increasing the total number of nodes. In the presented problem, it is no needed to increase the total number of nodes more than 100 in the GFD method because the accuracy of the results doesn't significantly increase for number of nodes more than 100.

To continue the analysis, it is assumed that the inner surface of the FGGPLs-reinforced thick hollow cylinder is excited by an axisymmetric shock loading as follows

$$F(t) = \begin{cases} \dfrac{\sigma_0}{t_s} t, & t < t_s, \\ \sigma_0, & t \geq t_s, \end{cases} \tag{92}$$

where t_s is an arbitrary reference time, which is assumed to be $t_s = 25\times10^{-6}$s. It is further assumed that σ_0 is equal to E_m, which is given as

$$\frac{\sigma_r(r_{in}, z, t)}{E_m} = \begin{cases} \dfrac{t}{t_s}, & t < t_s, \\ 1, & t \geq t_s. \end{cases} \tag{93}$$

Also, the length of the cylinder is considered to be very long. Consequently, at the middle point of the cylinder, the plane-strain condition can be assumed. The field variables are studied in detail in two parts including the wave propagation analysis and the time history analysis.

5.1 Wave propagation analysis

The wave propagation in terms of the non-dimensional radial displacement field can be found in Fig. 10. It can be observed that the wave front propagates with a finite speed along the radial direction. The variations of the non-dimensional radial displacement at various time instants can be seen in Fig. 10 for the type V of V_{GPL}, n = 2, z/L = 0.5 and W_{GPL} = 0.3%. The non-dimensional stress wave propagation along the radial direction of the FGGPLs-reinforced thick hollow cylinder is demonstrated in Fig. 11.

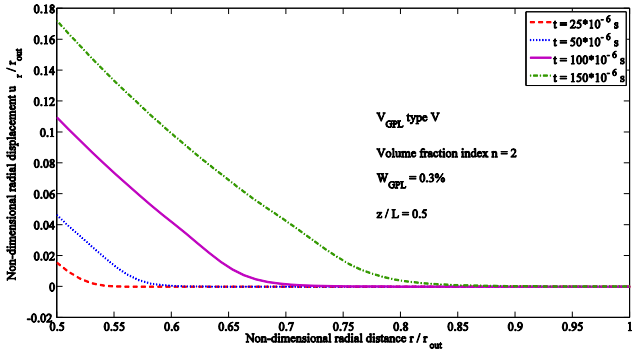

Fig. 10 The variations of the non-dimensional radial displacement along the radial direction at various time instants

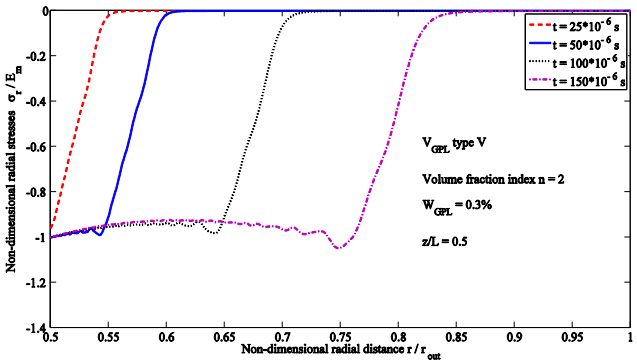

Fig. 11 The variations of the non-dimensional radial stress along the radial direction at various time instants

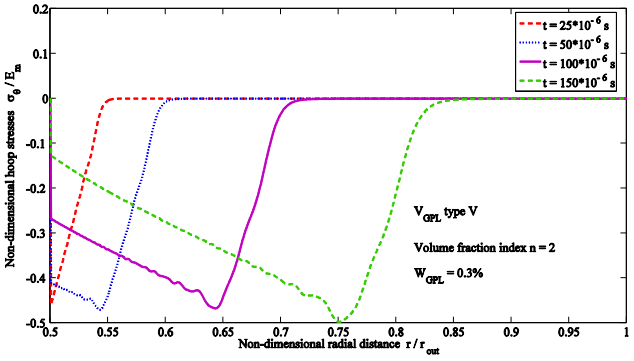

Fig. 12 The variations of the non-dimensional hoop stress along the radial direction at various time instants

The wave front can be tracked at various time instants. Also, it can be observed that the prescribed boundary conditions for the radial stresses are satisfied in a very good manner. The non-dimensional radial stress wave propagates with a finite speed along the radial direction. Also, Fig. 11 demonstrates the variations of the non-dimensional radial stress along the radial direction of the FGGPLs-reinforced thick hollow cylinder. The variations of the hoop stresses along the radial direction are obtained at various time instants, which are demonstrated in Fig. 12 for the same parameters as in Fig. 10. Here, it is also possible to track the propagation of the non-dimensional hoop stress wave at various time instants.

The effects of the volume fraction index n on the variations of the non-dimensional radial displacement, radial and hoop stresses can be revealed by using Figs. 13-15, respectively. It can be observed that when the value of n is increased, the values of the non-dimensional radial displacement, radial and hoop stresses are decreased for the type V of V_{GPL}. The similar behaviors are observed for the types Λ and X of V_{GPL}. It can be also concluded from Figs. 14 and 15 that the wave propagation velocities of both the non-dimensional radial and hoop stresses fields decrease when the value of n increases. The figures clearly depict that the wave fronts for small values of n are located before the other wave fronts for bigger values of n. It means that the non-dimensional radial and hoop stress waves propagate faster when the value of n decreases. The similar behaviors

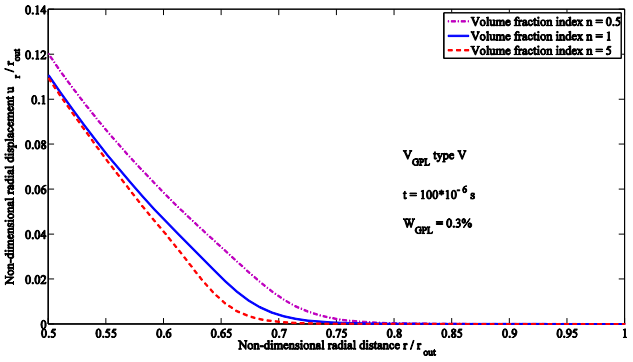

Fig. 13 The variations of the non-dimensional radial displacement along the radial direction for various values of the volume fraction index

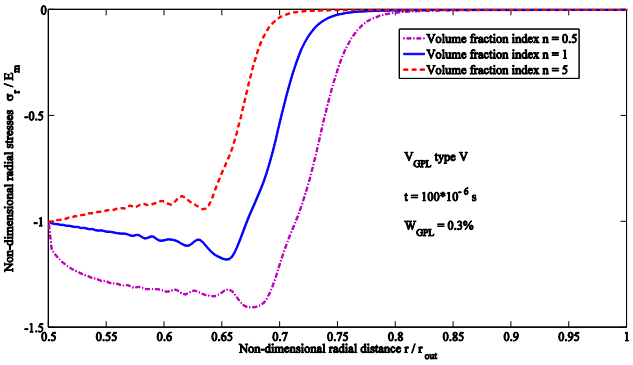

Fig. 14 The variations of the non-dimensional radial stress along the radial direction for various values of the volume fraction index

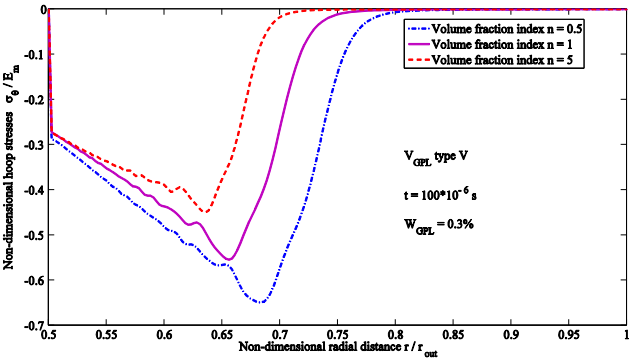

Fig. 15 The variations of the non-dimensional hoop stress along the radial direction for various values of the volume fraction index

can be seen for the types Λ and X of V_{GPL}. Fig. 16 shows the variations of the non-dimensional radial displacement along the radial direction for various types of V_{GPL} such as types V, Λ and X. The variations are presented for $n = 2$, $W_{GPL} = 0.3\%$ and $z/L = 0.5$ at $t = 100\times10^{-6}$s. Also, it is possible to see the effects of various types of V_{GPL} on the variations of the non-dimensional radial and hoop stresses, which are illustrated in Figs. 17 and 18, respectively. At the time instant $t = 100\times10^{-6}$, the maximum radial and hoop stresses are observed for the type X of V_{GPL}. Furthermore, it is

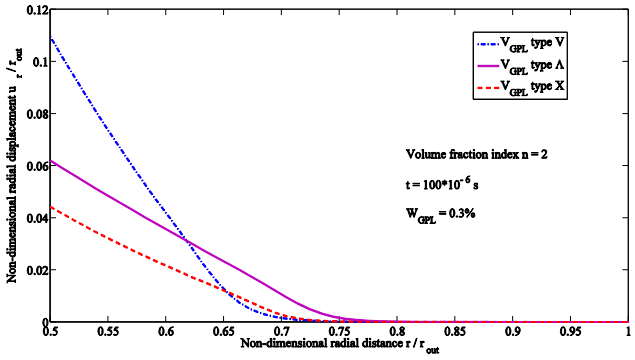

Fig. 16 The variations of the non-dimensional radial displacement along the radial direction for various types of the GPLs volume fraction

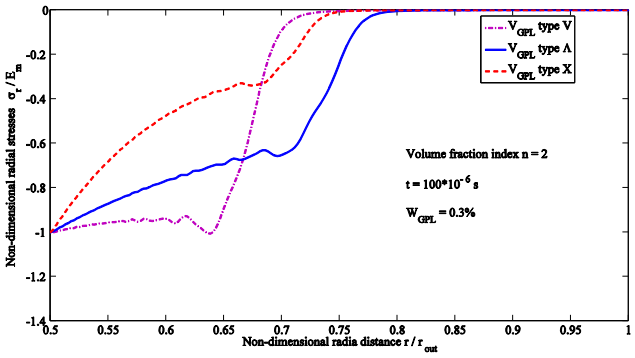

Fig. 17 The variations of the non-dimensional radial stress along the radial direction for various types of the GPLs volume fraction

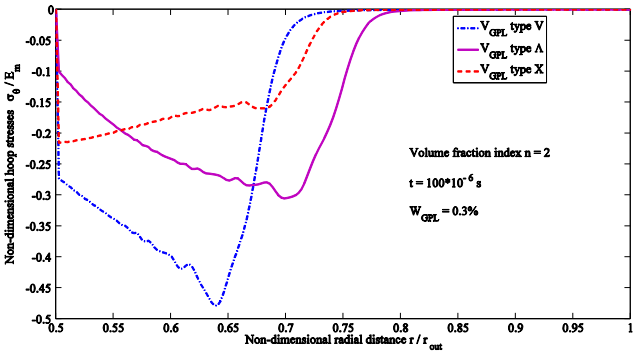

Fig. 18 The variations of the non-dimensional hoop stress along the radial direction for various types of the GPLs volume fraction

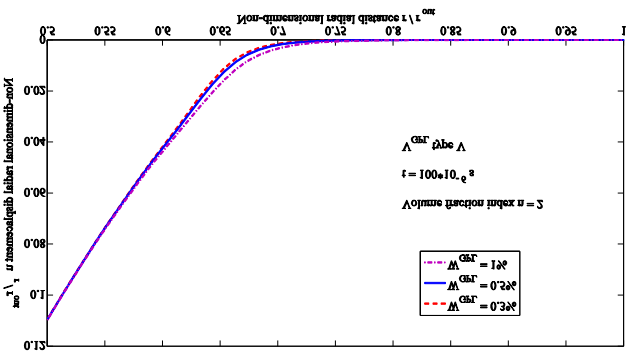

Fig. 19 The variations of the non-dimensional radial displacement along the radial direction for various values of W_{GPL}

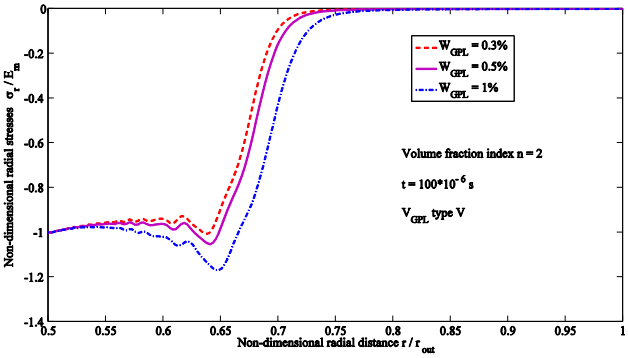

Fig. 20 The variations of the non-dimensional radial stress along the radial direction for various values of W_{GPL}

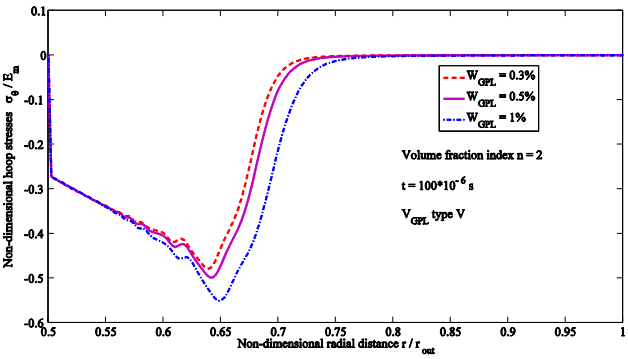

Fig. 21 The variations of the non-dimensional hoop stress along the radial direction for various values of W_{GPL}

possible to find the maximum stresses at various time instants for each type of V_{GPL} using the present meshless method.

The effects of the value of W_{GPL} on the variations of the field variables along the radial direction can be assessed by using Figs. 19-21, in which the variations of the non-dimensional radial displacement, radial and hoop stresses are illustrated for various values of W_{GPL}. Figs. 19-21 are given for $n = 2$, $z/L = 0.5$ at $t = 100\times10^{-6}$s in the case of the type V of V_{GPL}. It can be seen that the variation in the value of W_{GPL} influences the non-dimensional radial and hoop stresses more than the radial displacement. Also, it can be concluded that when the value of W_{GPL} is increased, the velocities of the non-dimensional radial and hoop stresses wave propagations are increased too. It means that the value of W_{GPL} influences directly the velocity of the wave propagation in the FGGPLs-reinforced thick hollow cylinder. In addition, it is observed that when the value of W_{GPL} is increased, the maximum values of the non-dimensional radial and hoop stresses are increased.

5.2 Time history analysis

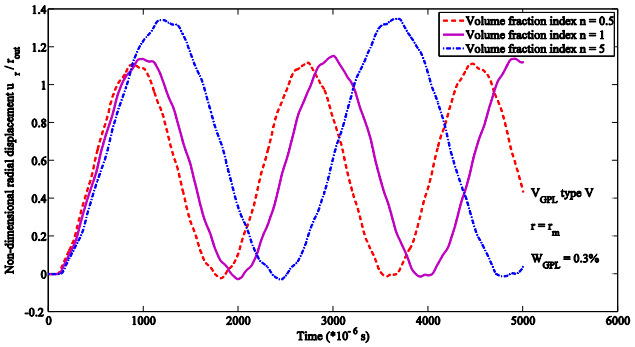

Fig. 22 The time histories of the non-dimensional radial displacement for various values of the GPLs volume fraction index

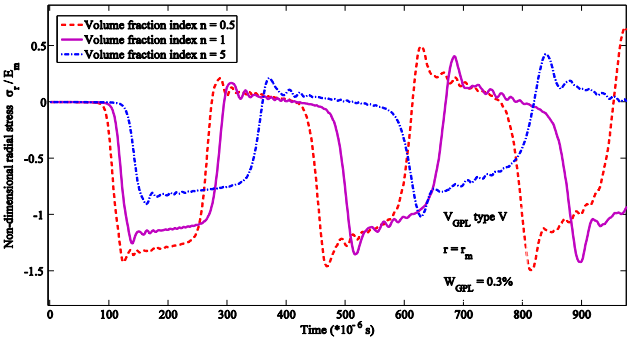

Fig. 23 The time histories of the non-dimensional radial stress for various values of the GPLs volume fraction index

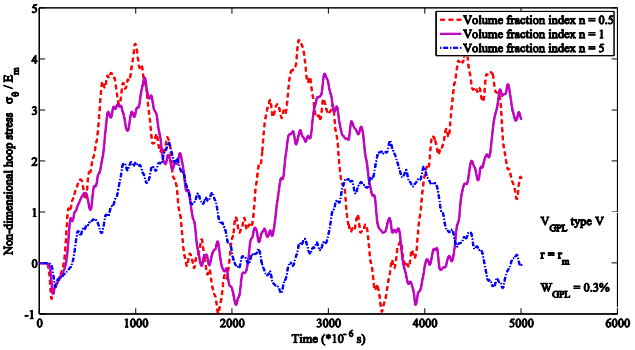

Fig. 24 The time histories of the non-dimensional hoop stress for various values of the GPLs volume fraction index

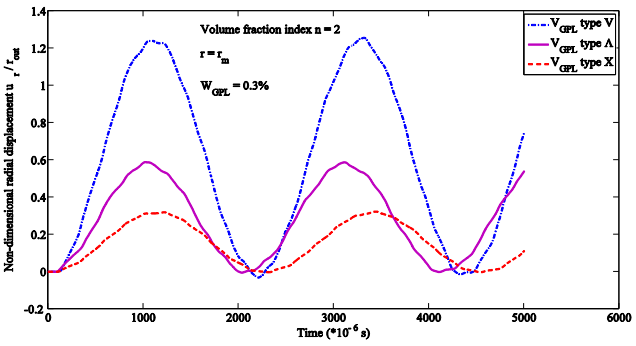

Fig. 25 The time histories of the non-dimensional radial displacement for various types of the GPLs volume fraction

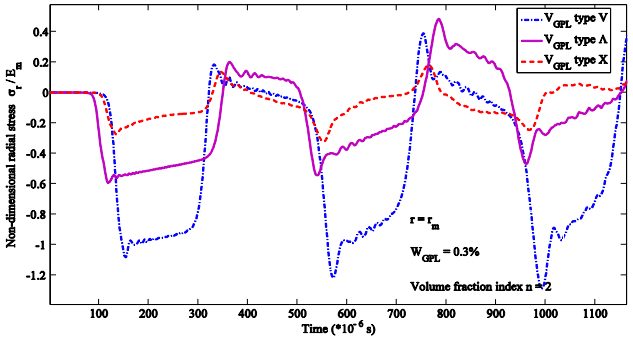

Fig. 26 The time histories of the non-dimensional radial stress for various types of the GPLs volume fraction

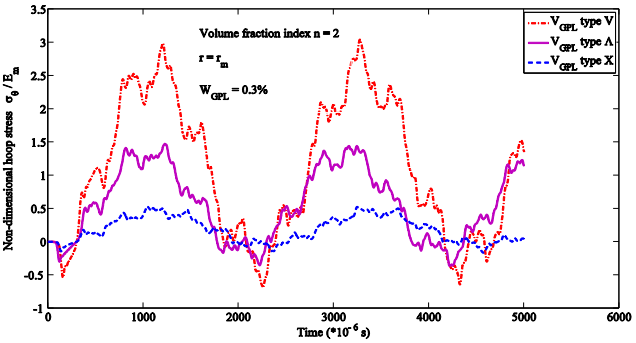

Fig. 27 The time histories of the non-dimensional hoop stress for various types of the GPLs volume fraction

The vibration behaviors of the considered cylinder can be observed in the time histories of the non-dimensional radial displacement, radial and hoop stresses, which are drawn in Figs. 22-24, respectively. Fig. 22 shows the time histories of the non-dimensional radial displacement for various values of the GPLs volume fraction index. The amplitude of the vibration in Fig. 22 increases with increasing value of n. The effects of the variation in the value of n on the time histories of the non-dimensional radial and hoop stresses can be analyzed by using Figs. 23 and 24. It is clearly observed that when the value of the GPLs volume fraction index increases the amplitude of the vibration and the maximum values of the non-dimensional radial and hoop stresses decrease. Figs. 22-24 are presented for $r = r_m$, $z/L = 0.5$ and $W_{GPL} = 0.3\%$ for the case of the type V of V_{GPL}. The effects of various types of V_{GPL} on the time histories of the field variables are presented in Figs. 25-27. The type V of V_{GPL} leads to the maximum values in the time histories of the non-dimensional radial displacement, radial and hoop stresses at a point with $r = r_m$ and $z/L = 0.5$. It can be observed that the various types of V_{GPL} don't have any significant effect on the vibration frequency in Figs. 25-27.

Figs. 28-30 show the time histories of the non-dimensional radial displacement, radial and hoop stresses, respectively, for various values of W_{GPL}. Using Figs. 28-30,

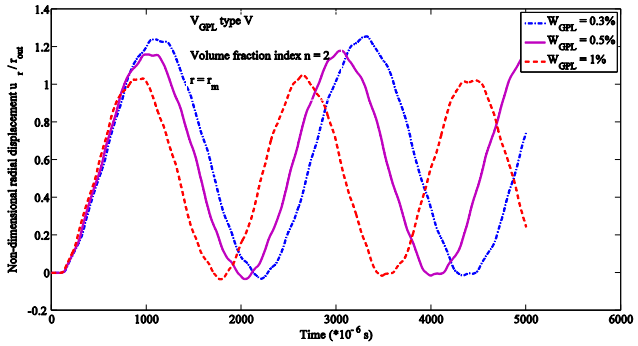

Fig. 28 The time histories of the non-dimensional radial displacement for various values of W_{GPL}

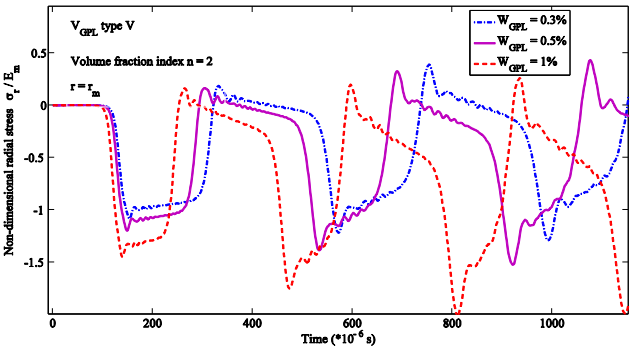

Fig. 29 The time histories of the non-dimensional radial stress for various values of W_{GPL}

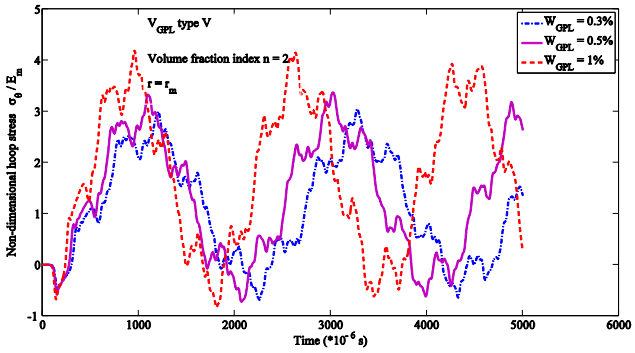

Fig. 30 The time histories of the non-dimensional hoop stress for various values of W_{GPL}

it is possible to study the effects of the variation in the value of W_{GPL} on the time histories of the field variables. When the value of W_{GPL} increases, the amplitude of the vibration and the peak values in the time history diagrams decreases for the non-dimensional radial displacement but increases in the time histories of the non-dimensional radial and hoop stresses. It can be concluded that when the value of W_{GPL} increases, the vibration frequency increases too in Figs. 28-30. The time histories of the non-dimensional radial displacement, radial and hoop stresses at various points of the FGGPLs-reinforced thick hollow cylinder are presented in Figs. 31-33. Here, three points are selected with $z/L = 0.5$ on various positions in the radial or thickness direction of the cylinder.

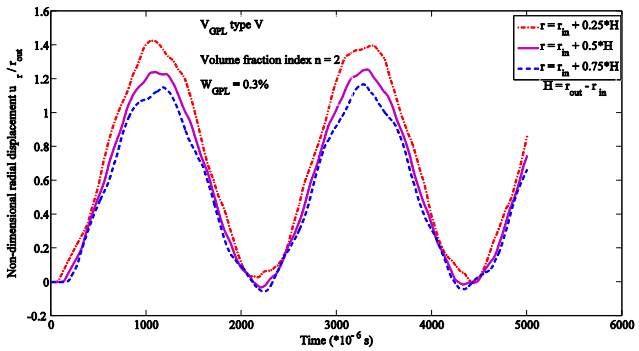

Fig. 31 The time histories of the non-dimensional radial displacement at several points in the thickness direction of the FGGPLs-reinforced composite cylinder

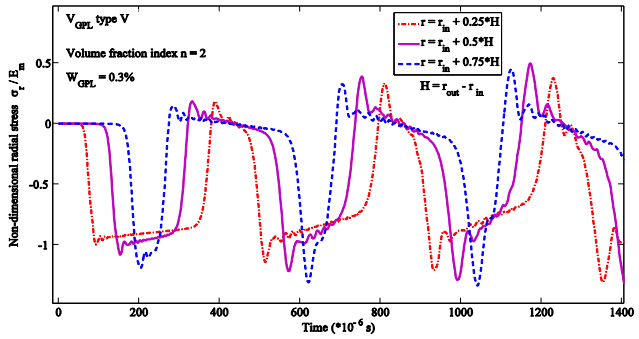

Fig. 32 The time histories of the non-dimensional radial stress at several points in the thickness direction of the FGGPLs-reinforced composite cylinder

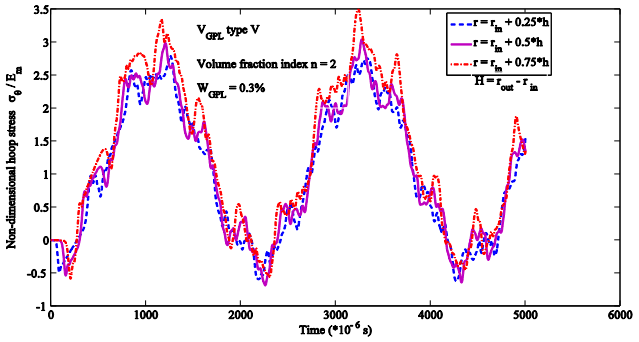

Fig. 33 The time histories of the non-dimensional hoop stress at several points in the thickness direction of the FGGPLs-reinforced composite cylinder

6. Conclusions

This paper deals with the wave propagation and time history analysis of the field quantities in a functionally graded graphene platelets-reinforced composite thick hollow cylinder subjected to a shock loading. The present study can be considered as a first attempt to employ a modified micromechanical model based on the nonlinear functionally graded distribution of the GPLs along the thickness of the composite cylinder in shock-induced dynamic analysis by using the meshless GFD method. For this purpose, a meshless GFD method is developed and

applied. The main results of the paper can be outlined as follows:

- A modified micromechanical model with various nonlinear grading patterns is presented to describe the nonlinear distribution of the GPLs along the radial direction of the nanocomposite thick hollow cylinders.
- The dynamic governing equations of the problem are derived based on the modified micromechanical model and discretized by the GFD method.
- The effects of several parameters on the wave propagation in both the displacement and stress fields are studied in detail. Using the modified micromechanical model and meshless GFD method, it is possible to track the wave fronts at an arbitrary time instant in both the displacement and stress fields.
- The time histories of the field variables are obtained and discussed for various parameters such as the type of V_{GPL}, GPLs volume fraction index and W_{GPL}.

The results show that the present meshless GFD method based on the modified micromechanical model has a high capability for wave propagation and dynamic analysis of the GPLs-reinforced cylinder structures.

Acknowledgments

The first author is grateful to Ferdowsi University of Mashhad for the financial support of the visiting scholarship at the Chair of Structural Mechanics, Department of Civil Engineering, University of Siegen, Germany.

References

Allahkarami, F., Nikkhah-Bahrami, M. and Ghassabzadeh Saryazdi M. (2017), "Damping and vibration analysis of viscoelastic curved microbeam reinforced with FG-CNTs resting on viscoelastic medium using strain gradient theory and DQM", *Steel Compos. Struct., Int. J.*, **25**(2), 141-155.

Benito, J.J., Urena, F., Gavete, L., Salete, E. and Muelas, A. (2013), "A GFDM with PML for seismic wave equations in heterogeneous media", *J. Comput. Appl. Math.*, **252**, 40-51.

Chavan, S.G. and Lal, A. (2017), "Bending behavior of SWCNT reinforced composite plates", *Steel Compos. Struct., Int. J.*, **24**(5), 537-548.

Chen, D., Yang, J. and Kitipornchai, S. (2017), "Nonlinear vibration and postbuckling of functionally graded graphene reinforced porous nanocomposite beams", *Compos. Sci. Technol.*, **142**, 235-245.

Duc, N.D., Cong, P.H., Tuan, N.D., Tran, P. and Thanh, N.V. (2017), "Thermal and mechanical stability of functionally graded carbon nanotubes (FG CNT)-reinforced composite truncated conical shells surrounded by the elastic foundations", *Thin-Wall. Struct.*, **115**, 300-310.

Elmarakbi, A., Jianhua, W. and Azoti, W.L. (2016), "Non-linear elastic moduli of graphene sheet-reinforced polymer composites", *Int. J. Solids Struct.*, **81**, 383-392.

Fan, C.M. (2015), "Generalized finite difference method for solving two-dimensional inverse Cauchy problems", *Inverse Probl. Sci. Eng.*, **23**(5), 737-759.

Fan, C.M., Huang, Y.K., Li, P.W. and Chiu, C.L. (2014), "Application of the generalized finite-difference method to inverse biharmonic boundary-value problems", *Numer. Heat Transfer, Part B*, **65**(2), 129-154.

Feng, C., Kitipornchai, S. and Yang, J. (2017a), "Nonlinear free vibration of functionally graded polymer composite beams reinforced with graphene nanoplatelets (GPLs)", *Eng. Struct.*, **140**, 110-119.

Feng, C., Kitipornchai, S. and Yang, J. (2017b), "Nonlinear bending of polymer nanocomposite beams reinforced with non-uniformly distributed graphene platelets (GPLs)", *Compos. Part B: Eng.*, **110**, 132-140.

Gavete, L., Urena, F., Benito, J.J. and Salete, E. (2013), "A note on the dynamic analysis using the generalized finite difference method", *J. Comput. Appl. Math.*, **252**, 132-147.

Ghayumizadeh, H., Shahabian, F. and Hosseini, S.M (2013), "Elastic wave propagation in a functionally graded nanocomposite reinforced by carbon nanotubes employing meshless local integral equations (LIEs)", *Eng. Anal. Bound. Elem. Method*, **37**, 1524-1531.

Ghouhestani, S., Shahabian, F. and Hosseini, S.M. (2014), "Application of meshless local Petrov-Galerkin (MLPG) method for dynamic analysis of multilayer functionally graded nanocomposite cylinders reinforced by carbon nanotubes subjected to shock loading", *CMES: Comput. Model. Eng. Sci.*, **100**(4), 295-321.

Gu, Y., Wang, L., Chen, W., Zhang, C. and He, X. (2017), "Application of the meshless generalized finite difference method to inverse heat source problems", *Eng. Anal. Bound. Elem.*, **108**, 721-729.

Hosseini, S.M. (2013), "Natural frequency analysis in functionally graded nanocomposite cylinders reinforced by carbon nanotubes using a hybrid mesh-free method", *CMES: Comput. Model. Eng. Sci.*, **95**(1), 1-29.

Hosseini, S.M. (2014a), "Elastic wave propagation and time history analysis in functionally graded nanocomposite cylinders reinforced by carbon nanotubes using a hybrid mesh-free method", *Eng. Computat.*, **31**(7), 1261-1282.

Hosseini, S.M. (2014b), "Application of a hybrid mesh-free method for shock-induced thermoelastic wave propagation analysis in a layered functionally graded thick hollow cylinder with nonlinear grading patterns", *Eng. Anal. Bound. Elem.*, **43**, 56-66.

Hosseini, S.M. (2015), "Shock-induced two dimensional coupled non-Fickian diffusion–elasticity analysis using meshless generalized finite difference (GFD) method", *Eng. Anal. Bound. Elem.*, **61**, 232-240.

Hosseini, S.M., Akhlaghi, M. and Shakeri, M. (2007), "Dynamic response and radial wave propagation velocity in thick hollow cylinder made of functionally graded materials", *Eng. Computat.*, **24**(3), 288-303.

Kiani, Y. (2016), "Shear buckling of FG-CNT reinforced composite plates using Chebyshev-Ritz method", *Compos. Part B: Eng.*, **105**, 176-187.

Kiani, Y. (2017), "Dynamics of FG-CNT reinforced composite cylindrical panel subjected to moving load", *Thin-Wall. Struct.*, **111**, 48-57.

Kitipornchai, S., Chen, D. and Yang, J. (2017), "Free vibration and elastic buckling of functionally graded porous beams reinforced by graphene platelets", *Mater. Des.*, **116**, 656-665.

Kumar, D. and Srivastava, A. (2016), "Elastic properties of CNT- and graphene-reinforced nanocomposites using RVE", *Steel Compos. Struct., Int. J.*, **21**(5), 1085-1103.

Lei, Z.X., Zhang, L.W. and Liew, K.M. (2017), "Meshless modeling of geometrically nonlinear behavior of CNT-reinforced functionally graded composite laminated plates", *Appl. Math. Computat.*, **295**, 24-46.

Phung-Van, P., Lieu, Q.X., Nguyen-Xuan, H. and Abdel Wahab, M. (2017), "Size-dependent isogeometric analysis of functionally graded carbon nanotube-reinforced composite nanoplates", *Compos. Struct.*, **166**, 120-135.

Shokravi, M. (2017), "Buckling of sandwich plates with FG-CNT-reinforced layers resting on orthotropic elastic medium using Reddy plate theory", *Steel Compos. Struct., Int. J.*, **23**(6), 623-631.

Song, M., Kitipornchai, S. and Yang, J. (2017), "Free and forced vibrations of functionally graded polymer composite plates reinforced with graphene nanoplatelets", *Compos. Struct.*, **159**, 579-588.

Verma, D., Gope, P.C., Shandilya, A. and Gupta, A. (2014), "Mechanical-thermal-electrical and morphological properties of graphene reinforced polymer composites: A review", *Transact. Indian Inst. Metals*, **67**(6), 803-816.

Vullo, V. (2014), *Circular Cylinders and Pressure Vessels*: *Stress Analysis and Designs*, Springer International Publishing, Switzerland.

Yang, J., Wu, H. and Kitipornchai, S. (2017), "Buckling and postbuckling of functionally graded multilayer graphene platelet-reinforced composite beams", *Compos. Struct.*, **161**, 111-118.

Zhang, L.W. (2017), "Mechanical behavior of laminated CNT-reinforced composite skew plates subjected to dynamic loading", *Compos. Part B*: *Eng.*, **122**, 219-230.
DOI: 10.1016/j.compositesb.2017.03.041

Zhang, L.W., Liu, W.H. and Liew, K.M. (2016), "Geometrically nonlinear large deformation analysis of triangular CNT-reinforced composite plates", *Int. J. Non-Linear Mech.*, **86**, 122-132.

Zhang, L.W., Liu, W.H. and Xiao, L.N. (2017a), "Elastodynamic analysis of regular polygonal CNT-reinforced composite plates via FSDT element-free method", *Eng. Anal. Bound. Elem.*, **76**, 80-89.

Zhang, L.W., Song, Z.G., Qiao, P. and Liew, K.M. (2017b), "Modeling of dynamic responses of CNT-reinforced composite cylindrical shells under impact loads", *Comput. Methods Appl. Mech. Eng.*, **313**, 889-903.

CC